# Supporting Information

## Stylianopoulos et al. 10.1073/pnas.1213353109

### SI Materials and Methods

**Description of the Mathematical Model.** To gain insight into the shape of tumors after releasing the stress and estimate the growth-induced stress, we constructed a 3D finite element model of an entire tumor in COMSOL and implemented an existing theory of tissue growth that has been applied successfully in arteries and brain tissue (1–3).

The tissue grows according to a specified growth deformation gradient tensor, $\mathbf{F_g}$, and therefore, the complete deformation gradient tensor $\mathbf{F}$ consists of two components: the growth component $\mathbf{F}_g$ and the elastic component $\mathbf{F}_e$ (i.e., $\mathbf{F} = \mathbf{F}_e\mathbf{F}_g$). As a first approximation, we assumed a volumetric and isotropic growth of the tumor with $\mathbf{F}_g = \lambda_g\mathbf{I}$, where $\lambda_g$ is the growth stretch ratio (3). We also made the assumption that the tumor behaves as a hyperelastic compressible neo-Hookean material with strain energy density function, $W$, given by (Eq. **S1**)

$$W = 0.5\left(\mu(-3 + \mathrm{II}_1) + \kappa(-1 + J_e)^{-2}\right), \qquad \textbf{[S1]}$$

where $\mu$ and $\kappa$ are the shear and bulk modulus of the material, respectively, and $J_e$ is the determinant of the elastic deformation gradient tensor $\mathbf{F}_e$. $II_1 = I_1 J_e^{-2/3}$, where $I_1$ is the first invariant of the right Cauchy–Green deformation tensor. This equation does not account for any transient poroelastic behavior. Finally, the Cauchy stress tensor is given by (Eq. **S2**)

$$\boldsymbol{\sigma} = J_e^{-1}\mathbf{F}_e\frac{\partial W}{\partial \mathbf{F}_e^T}. \qquad \textbf{[S2]}$$

More details about the implementation of the model can be found in refs. 2 and 4.

In the present study, we used values of the parameters $\mu$ and $\kappa$ for several tumor types measured previously and presented in Table S1 (5, 6).

Previous studies have shown a uniform compressive stress in the intratumoral region that turns to tensile stress at the margin (6, 7). Therefore, we assumed that a thin layer at the tumor periphery is in tension, whereas the intratumoral region is in compression. Furthermore, the growth and thus, the distribution of the stress are taken to be uniform throughout the intratumoral region and the periphery, but the growth stretch ratio $\lambda$ between these two regions is different.

The deformation of the tumor after a cut depends on the relative growth and stiffness between the intratumoral region and the peripheral layer (i.e., $\lambda_g^* = \lambda_{gt}/\lambda_{gc}$ and $\mu^* = \mu_t/\mu_c$, where the subscripts $t$ and $c$ denote intratumoral region and peripheral layer, respectively). We did a parametric analysis of the simulation depicted in Fig. 1*C* in the text, which simulates the cutting mode that we used in our experimental procedure. We varied $\lambda_g^*$, $\mu^*$, the thickness of the peripheral layer $h$, and the depth of the cut $H$. Because of symmetry, we performed our analysis on one-quarter of the domain. We applied a stress-free boundary condition to the outer and inner free surfaces and a symmetry boundary condition to the inner symmetry planes, and we fixed the bottom edge of the tumor to keep it in place (Fig. S1).

Fig. S2 shows the deformation of the tumor for constant $\lambda_g^*$, $h$, $H$, and four values of $\mu^*$. In the plots, a positive deformation indicates opening of the tumor, whereas a negative deformation indicates bulging of the inner surface. As the peripheral layer becomes stiffer (i.e., $\mu^*$ decreases), the bulging of the inner surface increases, and the opening initially increases and then drops. Notice that bulging is observed only when the peripheral tumor layer is stiffer than the intratumoral region.

The deformation of the center line of the tumor is the dashed line in Fig. S3. We separately varied the parameters $\lambda_g^*$, $h$, $H$, or $\mu^*$ while keeping the other three constant. Fig. S4 depicts the predictions of the mathematical model. Increase in the growth stretch ratio $\lambda_g^*$ increases the opening of the tumor but does not affect the bulging of the inner surface (Fig. S4*A*). In contrast, changes in the stiffness of the peripheral layer can significantly affect both bulging and opening (Fig. S4*B*). Importantly, there is a maximum in tumor opening as $\mu^*$ decreases (peripheral layer stiffens). This intriguing finding is the result of two competing effects: the tension at the margin and the compression at the interior of the tumor. Hence, increase in the thickness of the peripheral layer would decrease opening and increase bulging (Fig. S4*C*). Finally, the depth of the cut affects both bulging and opening (Fig. S4*D*).

The parameter $\lambda_g^*$ describes the relative cell proliferation between the tumor periphery and interior. Measurements of the spatial distribution of cancer cell proliferation (8, 9) have shown that the proliferation rate is higher at the periphery of the tumor, where there are more blood vessels. The proliferation rate at the periphery can be two times as much as the rate at the center. In Fig. S5, we plot the circumferential compressive growth-induced stress at the interior of the tumor as a function of the relative growth, $\lambda_g^*$. As the relative growth increases, growth-induced stress increases as well.

In addition, we performed simulations keeping $\lambda_g^*$ constant and varying the relative stiffness $\mu^*$ between the interior and the periphery of the tumor (Fig. S6). Fig. S6 shows that stiffening of the tumor periphery has little effect on the intratumoral compressive growth-induced stress.

**Model Limitations.** Our mathematical approach to quantify stress in tumors is subject to several assumptions and limitations. The magnitude of the stress given by the model depends on the specified material properties and growth. The material properties that we used were based on previous measurements in our laboratory (5, 6), which are in the same range as in other published studies (10, 11). However, when depleting tumor constituents, the material properties change. Thus, as discussed in the text, in many cases, we compared normalized tumor openings rather than stress magnitudes because of the uncertainty of the material properties. In addition, we assumed an isotropic and uniform growth of the tumor and peripheral layer, which might not be true given its heterogeneous structure. This assumption is an approximation that we had to make because of the lack of any experimental findings of growth patterns in our tumor models. Also, we used the neo-Hookean constitutive equation to describe the mechanical behavior of tumors. Tumors, like most biological tissues, are complex, heterogeneous, and poroelastic structures, and an isotropic, continuum-level constitutive equation might not be sufficient to describe their mechanical response. Nonetheless, the model predictions were consistent with our cutting experiments, which suggest that our assumptions are reasonable. As more data become available, they can be easily incorporated into our current framework. Finally, another limitation of the model is that many different growth fields or combinations of growth patterns and material properties can give rise to similar residual stress distributions. Added to this information is the fact that the cutting experiment only eliminates most and not all of the stress, making it difficult to come up with a unique growth

pattern. Hence, the current results provide an estimate of the growth-induced stress in tumors.

**Quantification of Growth-Induced Stress Using the Mathematical Model.** To quantify the growth-induced stress from the opening measurements, we used the mathematical model, which was implemented in COMSOL using the finite element method. The tumors were represented as ellipsoids. The lengths of the three axes of the tumors, which we incorporated into the model, were measured after the tumors were excised and before performing the cutting experiment. We simulated the experiment using the material properties shown in Table S1. Although bulging of the inner surface was evident in all types of tumors, it was not possible to perform accurate measurements of the bulging. To estimate the compressive stress of the intratumoral region, we varied $\mu^*$ from 1/10, where bulging is first observed (Fig. S2), to 1/40, where the two inner surfaces are almost in contact, and we calculated the value of $\lambda_g^*$ that matched the experimentally measured tumor opening. Subsequently, knowing the growth stretch ratio, $\lambda_g^*$, we used our model to convert this stretch to growth-induced stress. The thickness, $h$, of the peripheral layer was set to 5% based on previous studies (6), and the depth of our cuts was 80% of tissue thickness. We followed the same methodology to quantify the compressive, growth-induced stress of the human tumors presented in Table S3. Human tumors were modeled as ellipsoids based on the dimensions in the three coordinate directions, and we used the material properties of the stiffest tumor shown in Table S1.

**Interstitial Fluid Pressure Measurement.** Interstitial fluid pressure (IFP) was measured with the wick-in-needle technique (12) before tumor excision. For each tumor, IFP was measured in at least two different tumor locations.

**Piezoelectric Probe Measurement.** We measured the combination of IFP and some component of solid stress using a piezoelectric probe (13). Briefly, we connected a Millar Mikro-Tip pressure catheter transducer (0.33-mm diameter, SPR-1000) to a PCU-2000 Pressure Control Unit and an ADInstruments PowerLab data acquisition system. After calibration, we placed the catheter using a 25-gauge needle to create a space in the tissue to insert the probe after needle withdrawal.

**Tumor Growth Rate Measurement.** Tumor planar dimensions $(x, y)$ were measured with a digital caliper every 2 d. The volume of the tumor was estimated by the expression $V = \frac{\pi}{6}(xy)^{3/2}$. Tumor doubling time, $T$, was calculated by fitting the equation $V = V_o 2^{t/T}$ to the experimental data.

**Collagenase, Hyaluronidase, and Diphtheria Toxin Treatment.** Bacterial collagenase from *Clostridium* histolyticum (C0773; Sigma-Aldrich) was prepared by dissolving 1 mg collagenase in 10 mL 50 mM TES buffer containing 0.36 mM calcium chloride, pH 7.4, at 37 °C. After excision, the tumor was placed in the collagenase solution remaining at 37 °C for 2 h before measurement. Hyaluronidase (H3506; Sigma-Aldrich) was administered i.p. 24 and 1 h before tumor excision; each time, it was administered in a volume of 0.1 mL/20 g body weight to provide an enzyme activity of 100,000 IU/kg (14).

Human cells are 1,000 times more sensitive to diphtheria toxin than murine cells and thus, can be depleted by diphtheria toxin in vivo in mice (15, 16). Mice were injected one time i.p. with 1 μg diphtheria toxin in 0.3 mL PBS (15). After 24 h, the tumor was excised to perform the measurement.

**Saridegib Treatment.** Male FVB and male SCID mice bearing orthotopic human pancreatic adenocarcinomas AK4.4 and Capan-2 were treated as described previously (17). Saridegib was dissolved in a 5% aqueous solution of hydroxypropil-β-cyclodextran. Accounting for the potency of the batch received, the resulting solution was 5 mg/mL. After sonication and vortexing, the solution was sterile-filtered; 40 mg/kg resulting drug were administered daily by gavage for 8 or 10 d in mice bearing AK4.4 or Capan-2, respectively.

**Immunofluorescence Staining, Imaging, and Analysis.** For frozen sections, staining was performed according to a previously described protocol (18, 19). Human vimentin staining was done only on frozen tissues according to a previously described protocol (16). After retro-orbital injection of biotinylated lectin 5 min before tumor removal (100 μL; Vector Labs), tissues were excised, fixed for 2–3 h in 4% formaldehyde in PBS, incubated in 30% sucrose in PBS overnight at 4 °C, and frozen in optimal cutting temperature compound (Tissue-Tek). Transverse tumor sections (40-μm thick) were immunostained with antibodies to endothelial marker CD31 and counterstained by mounting with DAPI-containing medium (Vectashield; Vector Labs). Collagen I staining was done on both frozen and paraffin embedded tissues. In both cases, collagen I was detected using the LF-67 antibody provided by Larry Fisher (National Institute of Dental Research, Bethesda, MD). For paraffin sections, slides were treated with 3% hydrogen peroxide before antigen retrieval with Target Retrieval Solution, pH 9 (DAKO). The slides were further treated with 0.05% trypsin before the primary antibody was applied.

Eight random images (four interior and four periphery images) at 20× magnification at a resolution of 1.3 pixels to micrometers were taken from each slide. Images of collagen- and vimentin-stained sections were analyzed by thresholding based on the average image intensity. The fraction of pixels above threshold was used as a measure of the content in each tumor. Nonviable tissue area was excluded from the analysis. For vascular analysis, vessels were segmented using a custom semiautomated tracing program developed in MATLAB (MathWorks), allowing the removal of structures under 30 pixels and regions of autofluorescence.

**Statistical Analysis.** The data are presented as means with SEs. Groups were compared using a Student $t$ test.


1. Rodriguez EK, Hoger A, McCulloch AD (1994) Stress-dependent finite growth in soft elastic tissues. *J Biomech* 27:455–467.
2. Taber LA (2008) Theoretical study of Beloussov's hyper-restoration hypothesis for mechanical regulation of morphogenesis. *Biomech Model Mechanobiol* 7:427–441.
3. Xu G, Bayly PV, Taber LA (2009) Residual stress in the adult mouse brain. *Biomech Model Mechanobiol* 8:253–262.
4. Alford PW, Humphrey JD, Taber LA (2008) Growth and remodeling in a thick-walled artery model: Effects of spatial variations in wall constituents. *Biomech Model Mechanobiol* 7:245–262.
5. Netti PA, Berk DA, Swartz MA, Grodzinsky AJ, Jain RK (2000) Role of extracellular matrix assembly in interstitial transport in solid tumors. *Cancer Res* 60:2497–2503.
6. Roose T, Netti PA, Munn LL, Boucher Y, Jain RK (2003) Solid stress generated by spheroid growth estimated using a linear poroelasticity model small star, filled. *Microvasc Res* 66:204–212.
7. Sarntinoranont M, Rooney F, Ferrari M (2003) Interstitial stress and fluid pressure within a growing tumor. *Ann Biomed Eng* 31:327–335.
8. Hermens AF, Barendsen GW (1967) Cellular proliferation patterns in an experimental rhabdomyosarcoma in the rat. *Eur J Cancer* 3:361–369.
9. Brammer I, Zywietz F, Jung H (1979) Changes of histological and proliferative indices in the Walker carcinoma with tumour size and distance from blood vessel. *Eur J Cancer* 15:1329–1336.
10. Samuel MS, et al. (2011) Actomyosin-mediated cellular tension drives increased tissue stiffness and β-catenin activation to induce epidermal hyperplasia and tumor growth. *Cancer Cell* 19:776–791.
11. Levental I, et al. (2010) A simple indentation device for measuring micrometer-scale tissue stiffness. *J Phys Condens Matter* 22:194120.
12. Boucher Y, Baxter LT, Jain RK (1990) Interstitial pressure gradients in tissue-isolated and subcutaneous tumors: Implications for therapy. *Cancer Res* 50:4478–4484.
13. Provenzano PP, et al. (2012) Enzymatic targeting of the stroma ablates physical barriers to treatment of pancreatic ductal adenocarcinoma. *Cancer Cell* 21:418–429.
14. Muckenschnabel I, Bernhardt G, Spruss T, Buschauer A (1998) Pharmacokinetics and tissue distribution of bovine testicular hyaluronidase and vinblastine in mice: An

attempt to optimize the mode of adjuvant hyaluronidase administration in cancer chemotherapy. *Cancer Lett* 131:71–84.
15. Padera TP, et al. (2004) Pathology: Cancer cells compress intratumour vessels. *Nature* 427:695.
16. Duda DG, et al. (2010) Malignant cells facilitate lung metastasis by bringing their own soil. *Proc Natl Acad Sci USA* 107:21677–21682.
17. Olive KP, et al. (2009) Inhibition of Hedgehog signaling enhances delivery of chemotherapy in a mouse model of pancreatic cancer. *Science* 324:1457–1461.
18. Pluen A, Netti PA, Jain RK, Berk DA (1999) Diffusion of macromolecules in agarose gels: Comparison of linear and globular configurations. *Biophys J* 77:542–552.
19. Znati CA, et al. (2003) Irradiation reduces interstitial fluid transport and increases the collagen content in tumors. *Clin Cancer Res* 9:5508–5513.

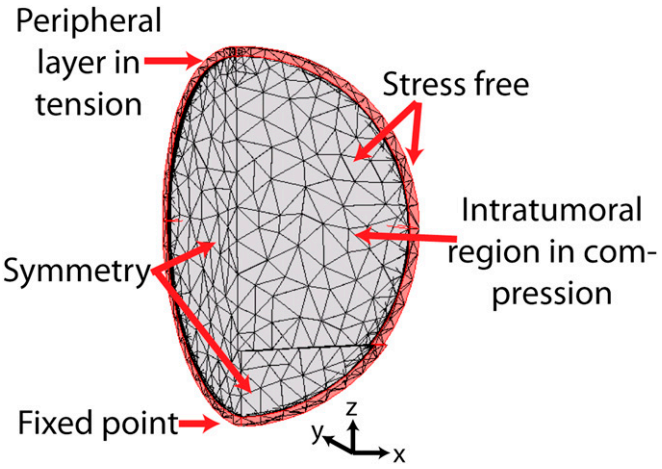


**Fig. S1.** Boundary conditions of the model. Because of symmetry, we solved for one-quarter of the domain; we applied symmetry boundary conditions at the planes of symmetry and stress-free boundary conditions at the free surfaces.

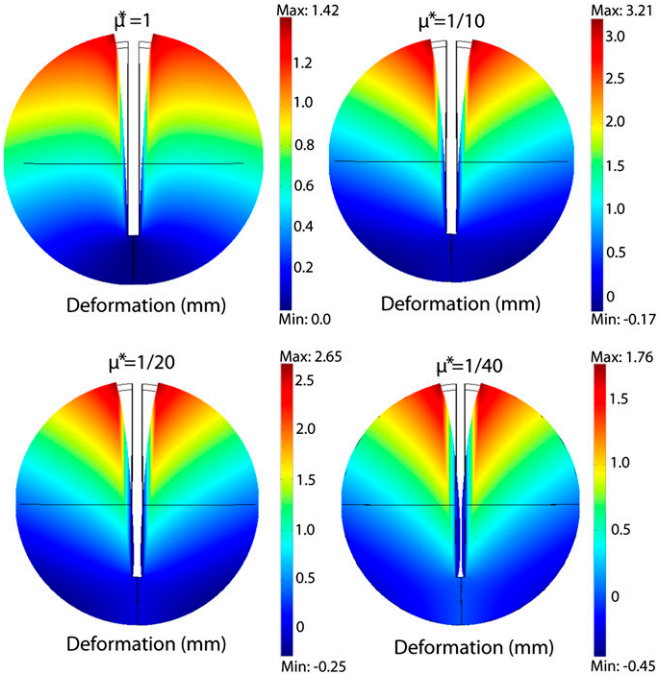


**Fig. S2.** Model predictions of the tumor shape after making a cut for four values of μ*. The value of $\lambda_g^*$ was 1.2, the peripheral layer occupied 5% of the thickness, and the depth of the cut was 0.8 cm.

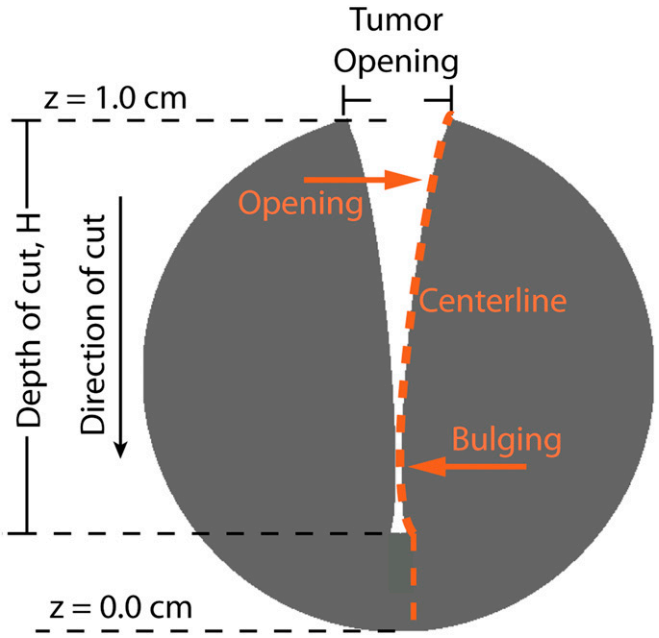


**Fig. S3.** Schematic of the deformation of the tumor after making a cut along one of its axes. The figure shows the centerline of the inner surface of the tumor that is presented in Fig. S4 and the tumor opening that was measured experimentally in Figs. 2–4.

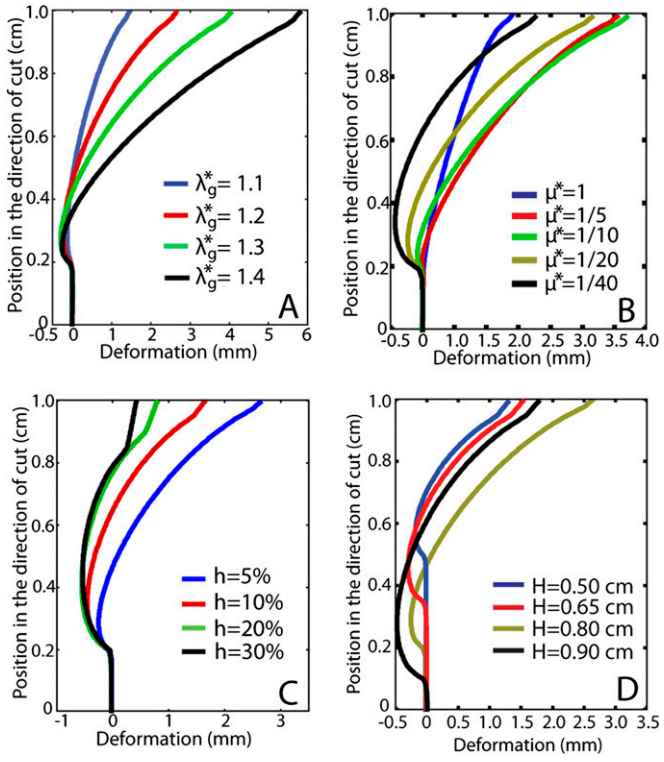


**Fig. S4.** Parametric analysis of the model predictions. The plots depict the deformation of the centerline of the inner surface of the tumor as shown in Fig. S3. (*A*) μ* = 1/20, *h* = 5%, and *H* = 0.8 cm. (*B*) $\lambda_g^* = 1.2$, *h* = 5%, and *H* = 0.8 cm. (*C*) $\lambda_g^* = 1.2$, μ* = 1/20, and *H* = 0.8 cm. (*D*) $\lambda_g^* = 1.2$, μ* = 1/20, and *h* = 5%.

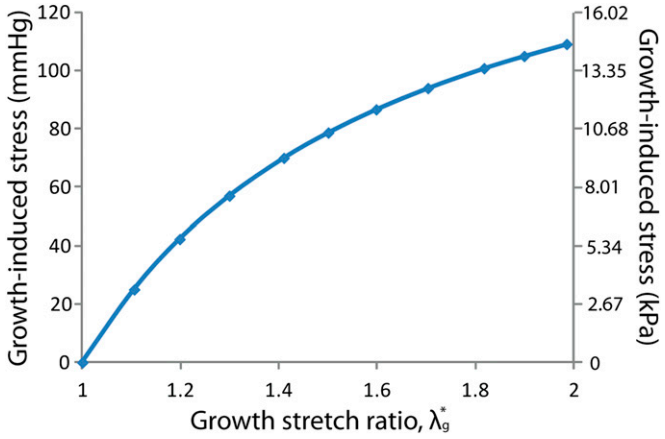


**Fig. S5.** Compressive circumferential growth-induced stress at the interior of the tumor as a function of the relative growth, $\lambda_g^*$. The shear modulus, $\mu$, of the interior was set constant to 150 mmHg, and the shear modulus, $\mu$, of the periphery was set constant to 3,000 mmHg.

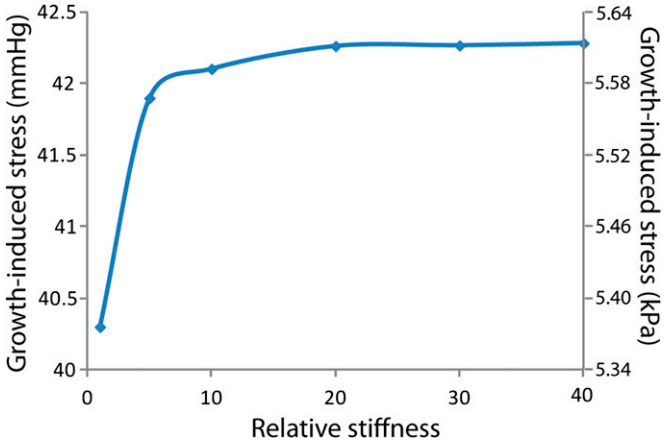


**Fig. S6.** Compressive circumferential growth-induced stress at the tumor interior as a function of the relative stiffness between the tumor periphery and center. The stiffness (shear modulus) at the center was kept constant at 150 mmHg, and the stiffness at the periphery was increased from 150 to 6,000 mmHg. $\lambda^*$ was set constant to 1.2.

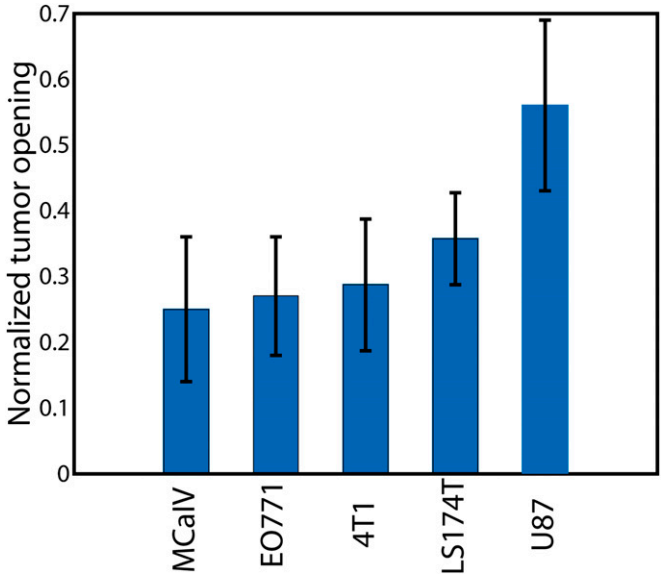


**Fig. S7.** Normalized tumor opening for five transplanted s.c. tumor models. The tumors grew on the flank of SCID mice. MCaIV, E0771, and 4T1 are murine mammary adenocarcinomas (breast tumors), LS174T is a human colon adenocarcinoma (colon tumor), and U87 is a human glioblastoma (brain tumor).

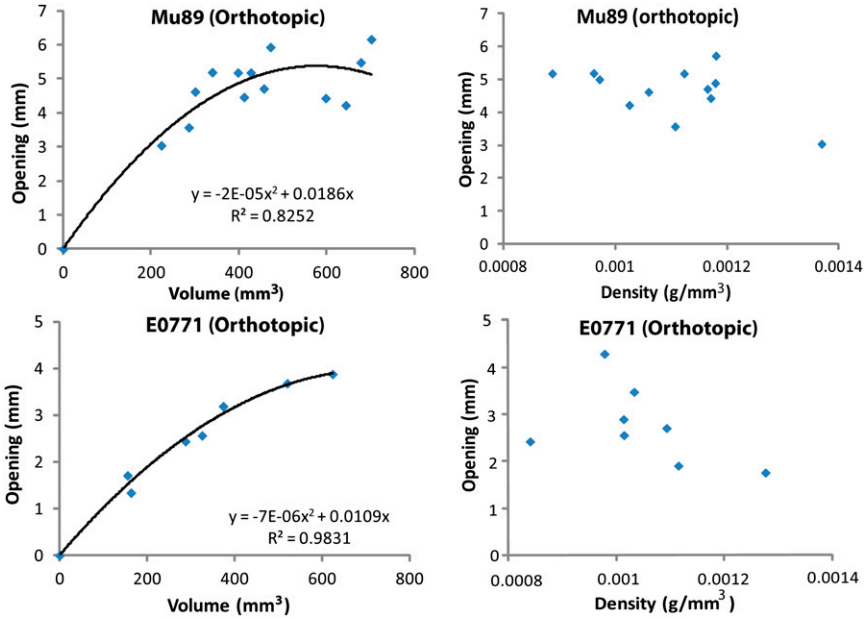


**Fig. S8.** Tumor opening as a function of tumor volume and mass density for two orthotopic cancer cell lines: Mu89 melanomas and E0771 mammary adenocarcinomas. Tumor opening increases linearly with volume before reaching a plateau. Higher volumes are usually correlated with increased necrosis, which is likely to reduce the interior swelling and thus, reduce the opening. No dependence of tumor opening on density was observed.

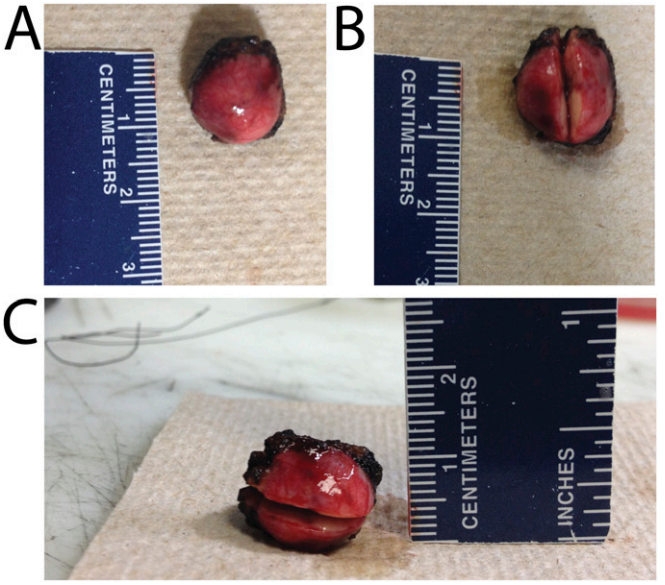


**Fig. S9.** Tumor opening of human pancreatic neuroendocrine tumors. A human pancreatic neuroendocrine tumor after it is excised from a patient before processing for histology (*A*) opens after a partial cut (*B*). The tumor opening is not affected after the tumor is placed on its side (*C*) or the tumor is closed manually.

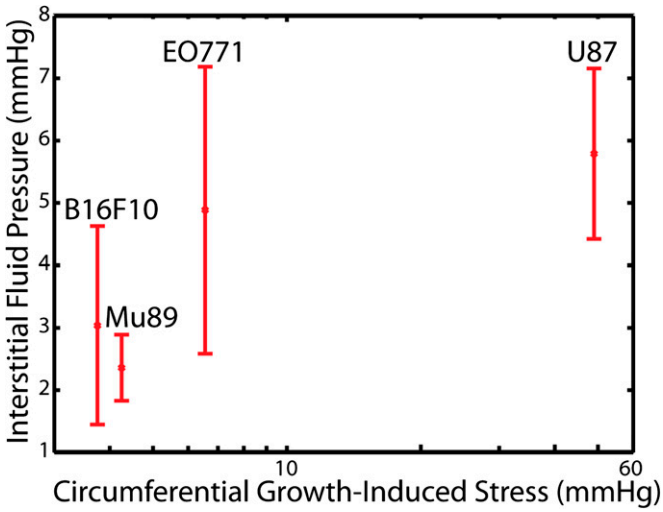


**Fig. S10.** IFP measurements of B16F10, Mu89, E0771, and U87 tumors. Although E0771 breast tumors exhibit less growth-induced stress than U87 gliomas, there is no statistically significant difference in their IFP ($P$ = 0.345).

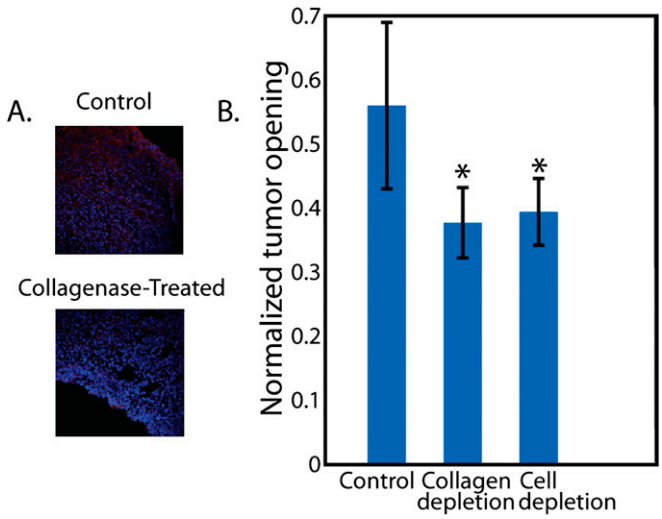


**Fig. S11.** (*A*) Treatment of U87 tumors with bacterial collagenase altered the collagen structure. Blue and red colors represent the nuclei and collagen, respectively. (*B*) Tumor opening of U87 glioblastoma implanted on the flank of SCID mice. Treatment with bacterial collagenase decreased the tumor opening significantly and thus, decreased the growth-induced stress ($P$ = 0.013). In addition, depletion of cancer cells with diphtheria toxin decreased the tumor opening significantly ($P$ = 0.026). The asterisks denote a statistically significant difference.

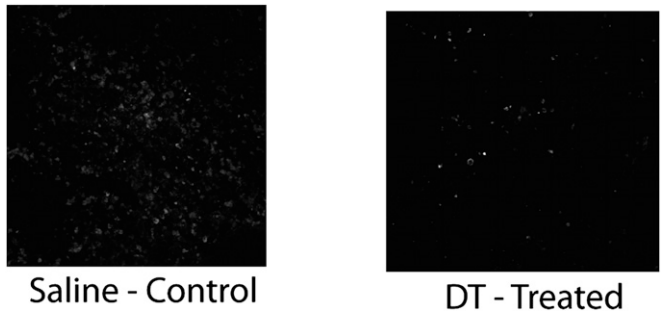


**Fig. S12.** Staining of E0771 tumors for colocalization of vimentin and alpha-smooth muscle actin (aSMA) confirms that human fibroblast levels were reduced by diphtheria toxin treatment. Representative images show that more human cells are intact in control compared with diphtheria toxin-treated tumors.

**Table S1. Mechanical material properties of the tumor types used in the study**

| Tumor type | Cancer cell line | Bulk modulus κ | | Shear modulus μ | |
|---|---|---|---|---|---|
| | | mmHg | kPa | mmHg | kPa |
| Epithelial | | | | | |
| Breast | MCaIV, 4T1, E0771 | 50 | 6.7 | 37.5 | 5.0 |
| Colon | LS174T | 30 | 4.0 | 22.5 | 3.0 |
| Pancreatic | Pan02, Capan-2, AK4.4 | Not available | Not available | Not available | Not available |
| Mesenchymal | | | | | |
| Sarcoma | HT1080 | Not available | Not available | Not available | Not available |
| Melanoma | Mu89, B16F10 | 19 | 2.5 | 14.25 | 1.9 |
| Glioma | U87 | 200 | 26.7 | 150 | 20.0 |

The shear modulus, μ, is a measure of the stiffness of the tumor (the higher the value of the shear modulus, the stiffer the tumor). The values of μ and κ shown here were measured experimentally in our previous work (1, 2). mmHg, millimeter of mercury; kPa, kilopascal.


1. Netti PA, Berk DA, Swartz MA, Grodzinsky AJ, Jain RK (2000) Role of extracellular matrix assembly in interstitial transport in solid tumors. *Cancer Res* 60:2497–2503.
2. Roose T, Netti PA, Munn LL, Boucher Y, Jain RK (2003) Solid stress generated by spheroid growth estimated using a linear poroelasticity model small star, filled. *Microvasc Res* 66: 204–212.


**Table S2. Experimentally measured doubling time and model estimates of the growth stretch ratio and growth-induced solid stress in the interior of the transplanted tumors used in the study**

| Cancer cell line | Doubling time (days) | Growth stretch ratio $\lambda_g^*$ (μ* = 1/10–1/40) | Compressive circumferential stress (μ* = 1/10–1/40) | |
|---|---|---|---|---|
| | | | mmHg | kPa |
| U87 (ectopic) | 5.18 | 1.17–1.32 | 38.0–60.1 | 5.07–8.01 |
| Mu89 | 2.13 | 1.15–1.29 | 3.2–5.3 | 0.43–0.71 |
| B16F10 | 0.94 | 1.13–1.25 | 2.8–4.7 | 0.37–0.63 |
| LS174T | 1.88 | 1.11–1.20 | 5.0–8.4 | 0.67–1.12 |
| E0771 (ectopic) | 2.21 | 1.08–1.14 | 4.9–8.2 | 0.65–1.09 |
| E0771 (orthotopic) | — | 1.13–1.25 | 7.4–12.4 | 0.99–1.65 |
| MCaIV (ectopic) | 2.50 | 1.07–1.13 | 4.5–7.4 | 0.60–0.99 |
| MCaIV (orthotopic) | — | 1.19–1.34 | 8.4–14.5 | 0.67–1.99 |
| 4T1 (ectopic) | 2.25 | 1.09–1.16 | 5.3–8.8 | 0.71–1.17 |
| 4T1 (orthotopic) | — | 1.11–1.20 | 6.3–10.5 | 0.84–1.40 |

Doubling time is a measure of tumor growth rate. High doubling times correspond to slow-growing tumors. The growth-induced solid stress in the tumor interior is compressive. The table shows the estimates of the growth-induced solid stress in the circumferential direction of the tumor. Material properties of pancreatic tumors and HT1080 soft-tissue sarcoma are not available, and analysis was not performed. mmHg, millimeter of mercury; kPa, kilopascal.

**Table S3. Dimensions and model estimates of the growth-induced solid stress developed in the interior of surgically excised human tumors along the circumferential direction**

| Tumor type | Tumor dimensions (cm) | Compressive circumferential stress | |
|---|---|---|---|
| | | mmHg | kPa |
| Breast tumor | 2.2 × 2.5 × 2.0 | 75.1–97.2 | 10.0–12.9 |
| Breast tumor | 2.6 × 2.7 × 1.6 | 99.5–142.4 | 13.3–19.0 |
| Pancreatic neuroendocrine tumor | 1.4 × 1.6 × 1.2 | 54.9–81.2 | 7.3–10.8 |
| Pancreatic neuroendocrine tumor | 1.3 × 1.8 × 0.9 | 16.4–31.2 | 2.2–4.2 |
| Osteosarcoma | 13.0 × 15.7 × 9.8 | 35.3–48.3 | 4.7–6.4 |
| Soft-tissue sarcoma | 5.0 × 5.9 × 3.1 | 73.7–107.6 | 9.8–14.3 |
| Soft-tissue sarcoma | 6.5 × 10.5 × 4.0 | 42.9–57.2 | 5.7–7.6 |
| Soft-tissue sarcoma | 12.0 × 15.0 × 6.0 | 50.8–58.5 | 6.7–7.8 |
| Liposarcoma | 6.2 × 6.9 × 6.8 | 41.8–58.7 | 5.6–7.8 |
| Neurofibrosarcoma | 8.5 × 12.0 × 8.0 | 45.6–62.3 | 6.1–8.3 |

The growth-induced solid stress in the tumor interior is compressive. The table shows the estimates of the growth-induced solid stress in the circumferential direction of the tumor. We used the mechanical properties of U87 tumors, the stiffest tumor in Table S1. mmHg, millimeter of mercury; kPa, kilopascal.

**Table S4. Comparison of IFP measured with the piezoelectric probe and wick-in-needle techniques**

| Method | Normal pancreas |
|---|---|
| Piezoelectric probe technique ($n$ = 4) | 9.8 (8.5–11.3) |
| Wick-in-needle technique ($n$ = 8) | −0.3 (−1.3–0.7) |

The gold standard wick-in-needle technique measures IFP only, whereas the piezoelectric probe measures IFP along with a component of solid stress. Values are given as mean (range) in millimeters of mercury.

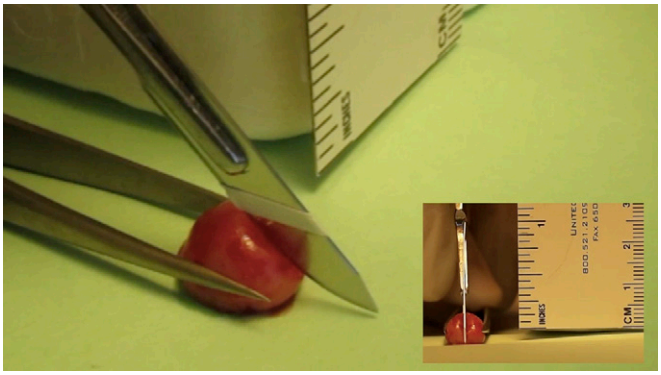

**Movie S1.** A freshly excised, orthotopically grown 4T1 breast tumor is cut. After the cutting is completed, the tumor is allowed to relax for 10 min. The real time is displayed on the left. Note the white tape of the scalpel. This tape was placed on the scalpel to indicate the depth of the cut in the tumor. This measurement assures that the tumor was cut 80% of its depth.

Movie S1

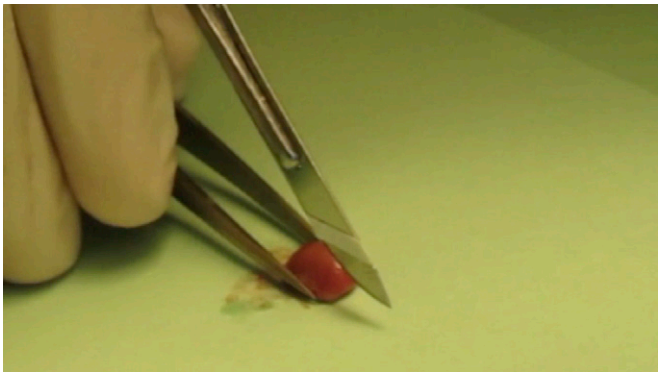

**Movie S2.** A freshly excised kidney from a female SCID mouse is cut using the same procedure used in the tumors. The kidney does not deform measurably.

Movie S2